Amorphization of a Proposed Sorbent of Strontium, Brushite, CaHPO4•2H2O, Studied by X-ray Diffraction and Raman Spectroscopy

Marie-Noëlle de Noirfontaine, Enrique Garcia-Caurel, Daniel Funes-Hernando, Mireille Courtial, Sandrine Tusseau-Nenez, Olivier Cavani, Jihane Jdaini, Céline Cau-Dit-Coumes, Frédéric Dunstetter, Dominique Gorse-Pomonti

Amorphization of a Proposed Sorbent of Strontium, Brushite, $CaHPO_4 \cdot 2H_2O$, Studied by X-ray Diffraction and Raman Spectroscopy

[1]Marie-Noëlle de Noirfontaine,[2]Enrique Garcia-Caurel, [2]Daniel Funes-Hernando,[1,3]Mireille Courtial, [4]Sandrine Tusseau-Nenez,[1]Olivier Cavani,[1,5]Jihane Jdaini, [5]Céline Cau-Dit-Coumes,[1]Frédéric Dunstetter,[1*]Dominique Gorse-Pomonti

[1]Laboratoire des Solides Irradiés, CNRS, Ecole polytechnique, CEA/DRF/IRAMIS, Institut Polytechnique de Paris, F-91128 Palaiseau, France

[2]Laboratoire de Physique des Interfaces et des Couches Minces, CNRS, Ecole polytechnique, Institut Polytechnique de Paris, F-91128 Palaiseau Cedex, France

[3]Université d'Artois, 1230 rue de l'Université, CS 20819, 62408 Béthune, France

[4]Laboratoire de Physique de la Matière Condensée, CNRS, Ecole polytechnique, Institut Polytechnique de Paris, F-91128, Palaiseau, France

[5]CEA, DES, ISEC, DE2D, Univ Montpellier, Marcoule, France

Corresponding author. Tel. +33 1 69 33 45 24; e-mail: dominique.gorse-pomonti@polytechnique.edu

Abstract

We present a systematic study of the transformation of brushite (dicalcium phosphate dihydrate, $CaHPO_4 \cdot 2H_2O$) under irradiation of electrons of well-defined energy (2.5 MeV) and flux as a function of the irradiation dose. Contrarily to model hydroxides such as portlandite and brucite, which are very resistant to electron radiation damage, the studied brushite decomposes quite easily, even for very low irradiation doses. Irradiated brushite samples were characterized using X-ray diffraction (XRD) and Raman spectroscopy to get complementary information about changes in atomic structure and chemical composition respectively under irradiation. XRD showed that irradiation causes a very limited dilatation of unit cell of crystalline brushite, which becomes progressively amorphous with increasing radiation dose. Raman spectroscopy complemented XRD results and confirmed that the transformation of brushite to the amorphous phase was not abrupt, but rather progressive. Raman spectroscopy allowed for the identification of the amorphous phase as a calcium pyrophosphate. Both techniques showed that the amorphization of brushite was not fully complete at the maximum dose used, 5.5 GGy (4 C). Interestingly, monetite phase, ($CaHPO_4$ dicalcium phosphate), was not detected at any step of the transformation as it is the case when brushite is thermally decomposed. This study reveals the high sensitivity to electron radiation of both hydrogen bonds and protonated phosphate units in brushite, thus facilitating the transformation into pyrophosphate. The damage of brushite by energetic electrons is to be carefully considered for applications related to the use of brushite as ion-exchanger in the decontamination of effluents polluted with strontium-90, an efficient beta ray emitter.

Keywords: Brushite, $CaHPO_4 \cdot 2H_2O$, calcium pyrophosphates, radiation damage, X-ray diffraction, Raman spectroscopy

1. Introduction

Cleaning operations during the dismantling of former nuclear facilities can produce highly radioactive and acidic effluents, mainly contaminated by cesium and strontium. These effluents first need to be partly decontaminated to comply with the activity acceptance criteria of existing aqueous waste treatment units usually designed for low- or intermediate-level radioactive waste. One way is to make them flow through columns filled with sorbents. Inorganic materials have been recently reported for the trapping of cesium in acidic medium [1, 2]. However, a solution is still lacking for strontium. Zeolites, titanates and silico-titanates commonly used to trap strontium in neutral or alkaline environment loose indeed their efficiency at low pH [3, 4]. A potential candidate under mildly acidic conditions might be brushite $CaHPO_4 \cdot 2H_2O$ (dicalcium phosphate dihydrate, DCPD). This mineral is stable at pH values within the range 2-6 [5] and several authors have shown that its crystalline structure can accommodate substitutions on its calcium sites [6, 7]. More precisely, Laniesse [8] has shown that strontium can substitute for calcium at Sr/Ca molar ratios below 0.3. The activity of the decontamination columns progressively increases under operation and can typically reach values as high as 0.5 TBq/kg. This raises the question of the stability of brushite under irradiation over the period of use of the columns (expected integrated dose of a few tenths to a few MGy), but also afterwards for the storage of the spent columns (expected integrated dose of several hundreds of MGy up to 1 GGy after 300 years).

In this context, we present here a preliminary study to the aim of evaluating how this compound, brushite, reacts under irradiation, even though the irradiation conditions, of course, remain far from the ones experienced during the decontamination and storage processes. The objective is to determine the sensitivity of this mineral to electron irradiation at "low" flux (in the range of 10^{13} to a few 10^{14} $e^-.cm^{-2}.s^{-1}$), using the beam delivered by a linear electron accelerator.

The crystal structure, sketched on Fig. 1, reveals that brushite has a layered structure parallel to the (**a**,**c**) monoclinic planes, consisting of alternate corrugated layers made of CaO_8 polyhedra and phosphate tetrahedra forming zig-zag chains parallel to the **a** axis [9]. The interlayer bonding consists of hydrogen bonds, labelled here as ---, associated to water molecules (O3---H2-O5), and (O1---H4-O6), which essentially lie along the **b** axis. The bending angle of the O3---H2-O5 and O1---H4-O6 elements are 172.8° and 169.2° respectively. Hydrogen bonding distorts the geometry of the water, giving rise to two distinct types of water: (H2-O5-H3) and (H5-O6-H4) which are labeled here as water 1, w_1, and water 2, w_2, respectively. The bending angle of w_1 and w_2 are 107.9° and 102.5° respectively. This angle is to be compared to the bending angle of 104.5° for free water molecules. Within the corrugated layers, the phosphate tetrahedra are bound together by hydrogen bonds of O1-H1---O4 type, and the CaO_8 polyhedra are bound together by hydrogen bonds of O3---H3-O5 type.

In a fundamental approach, there are three different damage mechanisms (ballistic, radiolytic and hydrogen – related) that may possibly contribute, the situation is as follows. We know that the maximum expected cumulated damage due to ballistic collisions during irradiation in our experiment should not exceed a few 10^{-4} displacements per atom (dpa) [10], in this case as in a number of non – metallic compounds. In other words, it means that it would remain about three orders of magnitude lower than the displacement damage required to cause a significant perturbation of their atomic structure or even amorphize them, the amorphization dose approaching ~1 dpa around room temperature, which can be achieved easily by ion – irradiation [11-13] or also by using the "high" flux of a transmission electron microscope [14]. Therefore, a priori, ballistic collisions should be expected to contribute only marginally to the overall damage in our experimental conditions. Radiolytic damage consists of the conversion of electronic excitations into atomic displacements taking the form of point defects or of some more severe structural disorder. The precise mechanisms that take place in a radiolytic process are rather complex and we do not have any means to model them in the framework of a brushite crystal. In this context, it

is impossible to decide whether or not radiolytic processes are involved in the possible transformation of brushite under electron radiation. A similar situation occurs with the third damage mechanism, related to hydrogen bonding, which cannot be disregarded since hydrogen bonding plays a key role to maintain the structure of brushite. Therefore, it seems likely that radiation mechanisms related to hydrogen bonding can play an important role. Facing the lack of theoretical support to understand electron-related damage mechanisms in brushite, we decided to start the study discussed in this paper using an empirical but systematic approach. We believe that the results of experiments, carried out in a particular range of electron energies, fluence and dose may bring some hints about the mechanisms taking place in the amorphization of brushite.

In this work, we choose irradiation conditions comparable to those already used to study the radiation damage effects on two model lamellar hydroxides, brucite, $Mg(OH)_2$, and portlandite, $Ca(OH)_2$ [10]. The powders are then analyzed by X-ray diffraction and Raman spectroscopy, revealing the ease of amorphization of brushite under the present irradiation conditions.

2. Experimental

2.1. Materials

A commercial powder of brushite (purity*:* ≥ 98%; Acros Organics) was used as the starting point material for all irradiation experiments. The main impurities present in the purchased powder, determined by X-ray fluorescence, were: Mg: 0.4 wt.% and Na: 0.5 wt.%. The particle size analysis by laser granulometry gives: d_{10} = 3.0 µm, d_{50} = 11.8 µm, d_{90} = 27.8 µm. Pellets of 13 mm diameter (1.33 cm^2) and ~ 1mm thickness were prepared from ~ 0.2 g of powder compressed for 60 seconds to 4.5 tons/cm^2 (~ 0.4 GPa).

2.2. Electron irradiation conditions

Electron irradiations at 2.5 MeV were performed using the accelerator NEC Pelletron of the SIRIUS platform (Ecole polytechnique, France) under helium gas at around 40°C. The beam current was kept fixed to 18 ± 2 µA. The corresponding flux was equal to ~8.5 x 10^{13} $e^-.cm^{-2}.s^{-1}$.The total inelastic energy loss $-\left[\frac{dE}{dx}\right]_{inel}$ and range were calculated using the ESTAR code [15].The values are reported in Table 1. We see that all electrons pass through the samples that are thus homogeneously irradiated. The dose rate was equal to about 25 kGy/s. The damage rate was roughly estimated of order ~ 1.7 x 10^{-9} dpa.s^{-1}. A set of irradiated samples was prepared using a wide variety of irradiation times, going from a few minutes (low irradiated samples) to a few days (highly irradiated samples). The fluences range between a few 2.3 x 10^{16} $e^-.cm^{-2}$ and 1.9 x 10^{19} $e^-.cm^{-2}$. The absorbed doses vary between 7 MGy and 5.5 GGy for the lowest and the highest irradiated samples respectively (Table 2). The irradiation temperature did not exceed ~ 44°C for the longest irradiation time.

2.3. Powder X-ray diffraction

X-ray diffraction (XRD) data were collected using a powder X-ray diffractometer (D8 Advance, Bruker) in the Bragg-Brentano geometry (θ/θ). The experimental configuration was set as follows: the incident X-ray beam (Cu radiation, 40 kV, 40 mA) passed through a fixed divergence slit of 0.5°, primary 1.5° axial Soller slits, and the diffracted beam went through a system of secondary 1.5° Soller slits before entering a fast 1D LynxEye XE-T detector (reduced energy discrimination window) of 2.915° (2θ) aperture. The instrument was operated in step-scan mode between 5° and 120° (2θ), with

0.007° (2θ) per step and 1s per step. An automatic anti-scattering knife was used to reduce unwanted scattered radiation by the atmosphere at low angles from the main beam. Before being measured, the pellets of virgin and irradiated brushite were slightly ground manually in an agate mortar. Then, the powders were compacted into the sample holder using the front-loading technique. Each scan was repeated three times to improve the signal-to-noise ratio. It was verified that pelleting caused only slight microstructural changes, and no phase transformation of the material.

Phase identification was carried out using Diffrac.EVA Suite (Bruker-AXS; V4.3, 2010-2018) and PDF-2 database (release 2009). Rietveld analysis was performed between 10° and 120° (2θ) using TOPAS software (BRUKER-AXS; V6, 2016) and ICSD database. For all adjustments, the refined parameters were the phase scale factors, sample displacement, background modeled by a Chebyshev polynomial combined with a 1/X term, unit cell and microstructural parameters. The crystallographic model of brushite, used as a starting point for the refinement was based on the structure proposed by Schofield et al. [9]. The atomic positions, site occupancies and temperature factors were kept constant during the refinement. Eventual preferred orientation of grains in the sample was taken into account using the March-Dollase correction [17]. Above 0.47 GGy (0.35C), a broad peak (modeled by a split pseudo-Voigt function), centered around 2θ = 29.4°, was added to reproduce a broad peak, typical of amorphous phases, which appeared in the experimental data as a background signal.

2.4. Raman spectroscopy

Raman measurements were performed at room temperature using a commercial confocal micro Raman spectrometer (LabRAMHR800 HORIBA JobinYvon) with a laser excitation wavelength of 405 nm (blue light) and equipped with a Peltier cooled CCD camera. Prior to each measurement, the spectrometer was calibrated and corrected against eventual drift using the 520.5 cm^{-1} line of a reference silicon nanocrystal. All spectra were recorded between 150 and 1200 cm^{-1}, with a spectral resolution of 2 cm^{-1}, using a 100x magnification microscope objective. The laser power measured on the focal point of the microscope objective at the sample surface was 0.12 mW. This low power level ensured that laser illumination did not modify the structure or composition of the sample during a full measurement run, which in general lasted for a few minutes. The raw Raman spectra were baseline corrected and normalized to the area under the peak at 585 cm^{-1}. As will be discussed further on, the peak at 585 cm^{-1} was the only one which was common to all samples discussed in this work. Baseline correction and normalization were done using the data treatment tools provided in the Orange/Quasar software [18-19]. In a second step, all the experimental spectra were fitted using a sum of Gaussian peaks in order to assign the different active vibrations present in the sample. Gaussian oscillators were used because they represented the experimental peak line shapes more accurately than Lorentz oscillators. In comparison to Voigt oscillators, Gaussian oscillators were preferred, since they need less parameters to be implemented in an automated data treatment code. The latter helps to reduce, at least in our case, numerical inaccuracies and fitted parameter cross-correlations during data fitting process. Data fit was performed with an in-house script written by the authors using Matlab software. The resulting best-fitted parameters, in particular the oscillator positions and intensities, allow for the identification of the different compounds present in the samples and also, they give an indication about the evolution of the transformation of brushite with irradiation dose.

Fluorescence was present in all measurements with an intensity characteristic of the measured sample. The fluorescence level, being minimal for virgin brushite, progressively augmented with the electron irradiation dose till a maximum level for the sample irradiated at 5.5 GGy (4 C). Although an extensive investigation of the fluorescence is not the subject of the present paper, we hypothesize that

the fluorescence level may be related to the density of defects created by electron irradiation in the samples. In order to minimize the effects of fluorescence-related artifacts in the Raman spectra, three laser sources were tested in a preliminary step: red (633 nm), green (520nm) and blue (405nm). From these three, the blue laser was retained since it minimized the overall fluorescence signal.

We compared two sample preparation protocols for Raman measurements. In both cases, the starting point was the same, a pressed pellet used for irradiation made of an agglomeration of fine grains (10 to 15 µm) that was partially broken in order to obtain small fragments. In the first protocol, the finest fragments were deposited on top of a silicon substrate, softly pressed with a spatula to flatten their surface and thus to minimize the intensity of scattered light in multiple directions, and then measured directly. In the second protocol, the fragments were suspended in absolute ethanol, and then a drop of the suspension was deposited on top of a gold coated glass substrate and left a few hours to dry. In both cases, measurements were done by focusing the laser beam on the surface of individual grains. It was experimentally found that measurements done on samples prepared following the suspension protocol showed better signal to noise ratio (around one order of magnitude), which indeed was more reproducible from grain to grain than samples deposited on silicon wafers without suspension. It was also found that there was no interaction between either, the sample and the gold substrate, or, the sample and the silicon wafer because, besides of a difference in the signal to noise ratio, the spectra of samples deposited either on gold or silicon substrates were comparable.

3. Results

The following section presents and discusses the results of the characterization using both XRD and Raman spectroscopy. The results of the two techniques are consistent, and show the progressive decomposition and amorphization of the initial crystalline brushite with the radiation dose. Moreover, Raman spectroscopy allowed the identification of the amorphous phase as a calcium pyrophosphate.

3.1. Powder X-ray diffraction

XRD shows that under the present irradiation conditions, brushite starts to lose its crystallinity during the first minutes of irradiation, for doses from 0.007 GGy (0.005 C). This is the first outcome of the XRD study.

The sequence of XRD patterns shows the evolution of the samples with increasing radiation dose (Fig. 2). The crystalline brushite phase in the virgin sample is unambiguously indicated by the presence of intense and sharp diffraction peaks. The identified crystalline phases and their respective proportions in the virgin sample are the following: brushite $CaHPO_4 \cdot 2H_2O$ (PDF-2 01-075-4374, ICSD 172258), 95.80wt.%; monetite $CaHPO_4$ (PDF-2 01-070-0359, ICSD917), 2.05 wt.%; and, newberyte $MgHPO_4 \cdot 3H_2O$ (PDF-2 01-070-2345, ICSD 8228), 2.15 wt.%. The experimentally determined parameters of the unit cell are: a = 5.8254 Å, b = 15.2135Å, c = 6.2565 Å, and β = 116.39°, which gives a theoretical volume of the unperturbed unit cell of V= 496.702 $Å^3$. The more intense peaks of monetite are clearly visible (see diffraction lines 002 and 200 at $2\theta_{Cu}$ = 26.35° and 26.606° respectively) [20]. We note that this compound was apparently difficult to detect in the eighties [21-22].

The intensity of all Bragg lines decreases and a broad diffuse peak appears near $2\theta_{Cu}$= 29.4° with increasing dose, showing that amorphization occurs progressively (Fig. 2.a). A decrease in the integrated intensity of all the Bragg lines is clearly observed with increasing dose, as also shown in Fig. 2.b for the

strongest diffraction line from the (020) planes parallel to the layers (normal to **b** axis) in the brushite structure (Fig. 1).

For a semi-quantitative analysis of the XRD data, we chose to represent in Fig. 3 the width (taken as the full width at half maximum, FWHM) of some representative diffraction peaks as function of the irradiation dose. From the data in the figure, it is interesting to notice a broadening of the diffraction peaks of brushite even for the lowest irradiation dose, 0.007 GGy (0.005 C). The broadening of the diffraction peaks increases with irradiation up to a dose of around 0.27 GGy (0.2 C). For higher doses, the diffraction peaks do not broaden any more, reaching a sort of plateau, which may imply that a maximum density of defects, or structural deformation, is attained. Besides, for doses higher than 0.27 GGy (0.2 C), a very broad peak typical of amorphous phases appears in the diffraction patterns (Fig. 2.a). Complete amorphization should be achieved around 5.5 GGy (4C) or slightly above, because traces of crystallinity remained observable at 5.5 GGy (4 C). The same broad peak centered at 29.4° has been observed in XRD measurements of amorphous calcium pyrophosphate by Gras *et al*. [23], which gives an interesting clue about the chemical composition of the amorphous phase. A relevant result that is worth mentioning here is that the diffraction peaks of monetite present in the virgin sample are no longer detected beyond 0.96 GGy (0.7 C). Further discussion about the identification of the amorphous phase will be provided in section 3.2.

In the following, we discuss the results of the Rietveld refinement analysis obtained for all doses up to 3.5 GGy (2.6 C). Note that the results of this study can be considered just as qualitative, owing to the presence of the amorphous bump and of a low angle diffuse scattering that both impact the fit. The unit cell volume increases with irradiation (Fig. 4) up to a radiation dose of around 0.27 GGy (0.2 C). For higher doses, it decreases progressively and recovers its initial value (V = 496. 667 $Å^3$) at about 1.8 GGy (1.3 C), but the unit cell is slightly different (a = 5.8170 Å, b = 15.2232 Å, c = 6.2575 Å, β = 116.32°).

An anisotropic expansion of the unit cell of the virgin brushite under irradiation is observed up to a maximum for a radiation dose of 0.27 GGy (0.2 C). Up to this dose, the unit cell dilation is similar to the one occurring when brushite is simply heated [9, 24], with a stronger increase in lattice parameters b and c compared to that of the lattice parameter a. The maximum variation of each lattice parameter is Δb= + 0.0125 Å, Δc= + 0.0102 Å, and Δa= + 0.0004 Å, which corresponds to a unit cell volume variation ΔV = +1.2248 $Å^3$. The maximum relative volume change, $\Delta V/V$ = +0.246%, achieved by the unit cell of the crystalline brushite is quite marginal when compared to the maximum expansion experienced by brushite under thermal treatment, 2.25 % at 400 K [9]. The maximum expansion under irradiation is equivalent to the one experienced under thermal treatment when the temperature of the sample is raised by only 25 K above room temperature. The difference between the evolution of brushite after thermal and irradiation treatments not only concerns the level of expansion achieved by the unit cell, but also the subsequent mineralogical transformation when the treatment is applied beyond the point of maximum expansion. For thermal treatments, and above 400 K, the crystallization water is lost and brushite transforms into an anhydrous crystalline phase, monetite ($CaHPO_4$), according to the reaction (Eq. 1) [25], whereas an amorphous product is formed by irradiation.

$$CaHPO_4 \cdot 2H_2O \rightarrow CaHPO_4 + 2H_2O \qquad \text{(Eq. 1)}$$

Moreover, for doses higher than 0.27 GGy (0.2 C), the amorphization process results in: i) a net decrease in the integrated intensity of the diffraction peaks of the remaining brushite without any further peak broadening, and ii) a decrease in the volume of the unit cell, which is distorted with respect to that of virgin brushite. Under the experimental conditions used for irradiation and analysis, the formation of

monetite, even as a transient product to the amorphous phase, is never detected, either by XRD or by Raman spectroscopy (see section 3.2). The transformation of brushite under electron irradiation is unexpected because the structural arrangement (zig - zag chains, corrugated interfaces between layers, interlayer hydrogen bonds) should be able to accommodate a more significant expansion of the structure as it is the case for thermal expansion. Under thermal treatment, the zig-zag chains become so separated from each other that the hydrogen bonds, which keep the structure in place, disappear, yielding free water which eventually evaporates, and monetite is formed. However, under irradiation, brushite decomposes when the chain separation is relatively small compared to that occurring after a thermal decomposition. Moreover, the fact that monetite does not form under irradiation indicates that the transformation mechanisms under thermal and irradiation treatments are very different from each other, and that something apparently happens in the chemical composition of brushite, leading to the formation of an amorphous phase under irradiation. This is the reason why we used Raman spectroscopy in combination to XRD to explore the changes in the chemistry of brushite.

3.2. Raman spectroscopy

Raman measurements were performed on a representative selection of the samples analyzed by XRD. In this section, two points are discussed: first, the evolution of the spectra with irradiation, showing the progressive transformation of brushite, and, second, the detailed analysis of spectra appertaining to the initial, intermediate and final state, in order to show how the composition of the phases present in the samples has changed.

Fig. 5 shows the resulting spectra after baseline correction and normalization from seven of the samples prepared for our study. Each spectrum was divided in two spectral windows to make easier the subsequent analysis and interpretation. The first spectral window, SPW1, goes from 300 to 650 cm^{-1}, and contains features related to the bending modes of the phosphate group. The second spectral window, between 650 and 1200 cm^{-1}, contains the stretching modes of the phosphate group. The transformation of brushite starts from the very beginning of the radiation exposure, as shown by the measured spectra, which features discrete yet noticeable changes in some of the peaks even at low radiation doses. As the radiation dose increases, some of the peaks shrink and broaden (for instance: peaks at 521 and 985 cm^{-1}), but others, not present in the virgin sample, become visible and grow (peaks at 351, 739, or 1038 cm^{-1} for instance). The spectrum of the virgin sample is comparable to the ones measured by other authors [26, 27, 28, 29], which confirms that our brushite is well identified by Raman spectroscopy. The spectrum of the sample treated with the highest dose of radiation significantly differs from that of virgin brushite, thus indicating that a major chemical and structural transformation has occurred. Similarly to XRD, the amorphous nature of the predominant phase in the sample is characterized by the large spectral width of some spectral features, that can be seen for instance in the spectrum of the sample irradiated at 5.5 GGy (4 C), and which contrasts with the sharp peaks in the spectrum of virgin brushite. After a systematic comparison of the spectrum of the sample irradiated at 5.5 GGy (4 C) with the Raman spectra found in the literature for different phases and compositions of calcium phosphates, it was found that it corresponds to that of amorphous calcium pyrophosphate [23, 30, 31]. It is thus assumed here that the most abundant phase in this sample may be a calcium pyrophosphate. Note that in XRD, the broad diffraction peak found at 29.4° (2θ) also corresponds to the one found for an amorphous calcium pyrophosphate. The fact that our results from XRD and Raman spectroscopy compare so well to the well characterized result supports our hypothesis that the amorphous phase formed after irradiation is a pyrophosphate. In an amorphous calcium pyrophosphate, the most prominent peaks related to the phosphate group appear at 351, 739, and 1038 cm^{-1}. All these characteristics are observed in the Raman spectrum of the sample irradiated at 5.5 GGy (4 C). The same spectrum also contains some spectral

features which correspond to peaks found in pure brushite. This fact seems to indicate that after receiving 5.5 GGy (4 C), the initial brushite is substantially transformed into a calcium pyrophosphate, but a residual amount of brushite still remains present in the sample.

A study of the evolution of the spectral features in the spectra of the different samples with electron radiation makes it possible to follow the details of the transformation of brushite into pyrophosphate. In what follows, the transformation of the spectra with the radiation dose is carefully investigated. The analysis of the spectra is divided in two parts corresponding to the two spectral windows above discussed and schematically shown in Fig. 6. Although the study is done for the seven samples, a particular attention is brought here to the virgin sample, the sample irradiated with the highest dose, 5.5 GGy (4 C), and a sample irradiated with 1.4 GGy (1 C), which represents an intermediate state of transformation of brushite to pyrophosphate.

In all cases, the considered spectrum was analyzed by adjusting an analytical function made of a sum of Gaussian peaks, each one representing a known referenced vibration mode in the bibliography, to the experimental intensity. Our goal was not to use the spectra to try to investigate the structure of the sample on the basis of group theory or other analytical method, but to verify whether the peaks found in the spectra corresponded to the vibration modes of well-characterized compounds. This strategy allowed for the identification of the chemical compounds present in the sample as well as the evolution of structure from one to another.

Spectral window 1- Deformation vibration modes. The spectrum of virgin brushite shows four well identified peaks corresponding to deformation modes of the O-P-O unit in the phosphate tetrahedron at 316, 379, 410 and 585 cm^{-1}respectively. The deformation vibration of the protonated unit O-P-OH in the phosphate tetrahedron appears at 521 cm^{-1} [28, 31]. In the sample irradiated at 5.5 GGy (4 C), two peaks are visible at 351 $cm^{-1}$and 484 cm^{-1}. The first peak corresponds to the bending of the unit P-O-P, which forms the bridge of the pyrophosphate anion between two phosphate tetrahedra. The second peak corresponds to a bending mode of the O-P-O unit located within the phosphate tetrahedra. The additional peak at 585 cm^{-1} corresponds to brushite which is still present in the sample. The spectrum of the sample irradiated at 1.4 GGy (1 C), is something in between the two preceding ones, and can be decomposed as a sum of peaks in the same positions as those found in brushite and pyrophosphate.

Spectral window 2 – Stretching vibration modes. The spectral features of virgin brushite in the spectral window from 650 to 1200 cm^{-1} correspond to stretching vibration modes of different bonds in the phosphate group, HPO_4^{2-}. The most prominent peak appears at 985 cm^{-1} and it is attributed by different authors [26, 30, 31], after group theory analysis, to the non-degenerated symmetric stretching mode of the P-O bonds in the phosphate group, HPO_4^{2-}. Close to this important peak, there is also a double peak, at 1057 and 1079 cm^{-1}, attributed to two distinct antisymmetric stretching modes of the P-O bonds in the HPO_4^{2-} group. There are also two more noticeable peaks at 876 and 1114 cm^{-1} attributed to symmetric and asymmetric modes of the P-OH unit in HPO_4^{2-} respectively. The weak peak at 819 cm^{-1} has also been observed by other authors [27, 28], although it has not been unambiguously assigned to a given vibrational mode.

The spectrum of the sample irradiated at 5.5 GGy (4 C) is also rich in spectral features which are clearly different from those of the virgin sample. The most visible peaks appear at 739 cm^{-1} and 1038 cm^{-1}. In crystalline pyrophosphate phases, there is a band appearing between 742 and 738 cm^{-1} which, after group theory analysis, is assigned to the symmetric stretching of the P-O-P unit, the bridge between two phosphates in the pyrophosphate anion [23]. By analogy, it is hypothesized here that the peak at

739 cm^{-1} may be related to the same type of vibration mode. This particular peak is not present in virgin brushite, and it clearly indicates the presence of the pyrophosphate in the irradiated samples because brushite has not any Raman active modes at 739 cm^{-1}. The relatively weak peak at 948 cm^{-1} can be attributed to the asymmetric stretching mode of the P-O-P unit. The most intense peak, at 1038 cm^{-1}, is also attributed to the symmetric stretching modes of the P-O bonds in the tetrahedra groups of the pyrophosphate anion. The position of this intense peak is different from that of the most important peak in brushite, at 985 cm^{-1}, which is a clear indication of the presence of different phases in the irradiated sample. The peaks at 1111 cm^{-1} and 1162 cm^{-1} have been attributed to asymmetric stretching modes of the P-O bonds in the tetrahedra groups of the pyrophosphate anion.

The spectrum of the sample irradiated at 1.4 GGy (1 C) shows an ensemble of spectral features which can be interpreted as a mixture of those of brushite and pyrophosphate. Typical peaks of pyrophosphate at 739, 948 and 1038 cm^{-1} can be easily identified, and also, characteristic vibrations of brushite at 876, 985, 1005, and 1079 cm^{-1} are also visible. It is interesting to note here that peaks at 1057 and 1079 cm^{-1} which are well separated in brushite, merge in a broader peak at 1065 cm^{-1}. The spectral features appearing in the sample irradiated at 1.4 GGy (1 C) suggest that brushite and pyrophosphate co-exist in the sample. In the absence of any visible spectral signature of an eventual third substance that would mediate the transition from pure brushite to a given pyrophosphate, it seems that the transition from one substance to the other is direct and progressive as a function of the radiation dose. The peaks at 1114 and 1163 cm^{-1} have been attributed to asymmetric stretching modes of the P-O bonds in the tetrahedra groups of the pyrophosphate anion.

The onset of the transformation of the brushite may be triggered by the accumulation of defects produced under electron irradiation. The evident decrease in the intensity of the different peaks associated to the vibrations of the HPO_4^{2-} group seems to indicate that hydrogen loss from the protonated phosphate tetrahedra is an important step for the transformation of brushite to pyrophosphate. The latter transformation mechanism is in contrast with the one occurring under thermal treatment, based on the loss of water after disparition of the hydrogen bonds between zig-zag chains. In our case, once hydrogen is lost, it seems plausible that two deprotonated phosphate tetrahedra link together, dimerize, to form a pyrophosphate anion $[P_2O_7]^{4-}$, thus opening the way to the formation of a calcium pyrophosphate. The progressive evolution of the spectra with radiation dose seems to indicate that the transformation from brushite to pyrophosphate is not an abrupt phase transition, but a gradual change that takes place as a consequence of the accumulation of electron collision related events in the material. Moreover, Raman spectroscopy helps to understand the decomposition mechanisms of brushite under irradiation and its ulterior transformation into an amorphous pyrophosphate. The progressive decline of Raman peaks associated to the HPO_4^{2-} group indicates that, contrarily to what happens under thermal treatment, the protonated phosphate seems to be highly sensitive to the defects generated by the electron beam.

4. Conclusions and Perspectives

In the present paper, we report the results of the study of the transformation of brushite under irradiation of electrons of well-defined energy and flux as a function of the irradiation dose (irradiation time). Contrarily to model hydroxides such as portlandite and brucite, the studied brushite decomposes quite easily under irradiation, even at very low doses. Irradiated brushite samples were characterized using XRD and Raman spectroscopy to get information about the atomic structure and chemical variations induced under irradiation respectively. XRD showed that the transformation starts from the very beginning of irradiation by an accumulation of defects and the dilation of the unit cell of the brushite crystal. Beyond 0.27 GGy (0.2 C) the unit cell of the irradiated material contracts, thus signing the increasingly proportion of the amorphous phase in the material compared to that of brushite. Raman

spectroscopy supports XRD in that the transformation of brushite to the amorphous phase is not abrupt, but rather progressive with irradiation dose. Raman spectroscopy allowed for the identification of the amorphous phase as a calcium pyrophosphate, and also, it showed that the transformation was not fully complete at the highest dose reached in the present study, 5.5 GGy (4 C). Comparison of the outcome of the transformation after either a thermal or an irradiation treatment of brushite showed net differences between them. While under thermal conditions, the water of crystallization in brushite is lost and the material transforms into monetite [27, 32], under irradiation conditions, the phosphate tetrahedra of brushite deprotonate, which induces the formation of pyrophosphate units.

In forthcoming research, Raman measurements will be combined to infrared, IR, and nuclear magnetic resonance spectroscopy, NMR, measurements in order to explore the vibrations related to water molecules. The combination of these techniques will make possible the study of the evolution of the water of crystallization with radiation dose, to get a deeper understanding of the role of hydrogen bonding in the transformation from brushite to pyrophosphate, and to complete the comparison between the thermal and irradiation induced transformations.

Our study showed the high sensitivity of hydrogen bonds in brushite to electron radiation and the ease of the transformation of brushite to pyrophosphate. The later characteristic is to be considered carefully for applications related to the use of brushite as ion-exchange material in the decontamination of water polluted with strontium-90, a powerful source of beta radiation. Although the radiation doses used in the present study are very high compared to those found in real polluted environments, to date, it is not known the impact, either positive or negative, that the partial transformation of brushite into pyrophosphate will have on the ability of the material to efficiently exchange calcium to strontium-90 cations.

5. Acknowledgements

The authors would like to thank the EMIR&A French accelerator network for radiation beam time. Moreover, also, the authors would like to acknowledge F. Borondics and C. Sandt from Synchrotron SOLEIL, France, for fruitful discussions on spectroscopic data treatment, and training on the use of Quasar software, as well as Y. Barré and A. Dannoux-Papin, from CEA, ISEC, France, for providing operational data about the radiological properties of decontamination columns.

6. References

[1] H. Mimura, N. Kageyama, K. Akiba, M. Yoneya, Y. Miyamoto, Ion-exchange properties of potassium nickel hexacyanoferrate (II) compounds, Solvent Extraction and Ion Exchange 16(4) (1998) 1013-1031. https://doi.org/10.1080/07366299808934566

[2] T.A. Todd, V.N. Romanovskiy, A comparison of crystalline silicotitanate and ammonium molybdophosphate polyacrylonitrile composite sorbent for the separation of cesium from acidic waste, Radiochemistry 47(4) (2005) 398-402. https://doi.org/10.1007/s11137-005-0109-3

[3] S.F. Yates, P. Sylvester, Sodium nonatitanate : a highly selective inorganic ion exchanger for strontium, Separation Science and Technology 36(5-6) (2001) 867-883. https://doi.org/10.1081/SS-100103625

[4] A. Merceille, Etude d'échangeurs d'ions minéraux pour la décontamination liquide en strontium, PhD thesis, University of Montpellier, France, 2012.

[5] S.V. Dorozhkin, Calcium orthophosphates, Journal of Material Science 42 (2007) 1061-1095. https://doi.org/10.1007/s10853-006-1467-8

[6] E. Rokita, C. Hermes, H.F. Nolting, J. Ryczek, Substitution of calcium by strontium within selected calcium phosphates, Journal of Crystal Growth 130(3-4) (1993) 543-552. https://doi.org/10.1016/0022-0248(93)90543-6

[7] M.H. Alkhraisat, F.T. Marino, C.R. Rodrıguez, L.B. Jerez, E. Lopez-Cabarcos, Combined effect of strontium and pyrophosphate on the properties of brushite cements, Acta Biomaterialia 4(3) (2008) 664-670. https://doi.org/10.1016/j.actbio.2007.12.001

[8] P. Laniesse, Les ciments brushitiques à base de wollastonite - Réactivité, propriétés et application au traitement et au conditionnement d'effluents contaminés par du strontium, PhD thesis, University of Montpellier, France, 2019.

[9] P.F. Schofield, K.S. Knight, J.A.M. van der Houwen, E. Valsami-Jones, The role of hydrogen bonding in the thermal expansion and dehydration of brushite, di-calcium phosphate dihydrate, Physics and Chemistry of Minerals 31 (2004) 606-624. https://doi.org/10.1007/s00269-004-0419-6

[10] M.-N. de Noirfontaine, L. Acher, M. Courtial, F. Dunstetter, D. Gorse - Pomonti, An X-ray powder diffraction study of damage produced in $Ca(OH)_2$ and $Mg(OH)_2$ by electron irradiation using the 2.5 MeV SIRIUS accelerator, Journal of Nuclear Materials 509 (2018) 78-93. https://doi.org/10.1016/j.jnucmat.2018.06.019

[11] L.W. Hobbs, F.W. Clinard, S.J. Zinkle, R.C. Ewing, Radiation effects in ceramics, Journal of Nuclear Materials 216 (1994) 291-321. https://doi.org/10.1016/0022-3115(94)90017-5

[12] S.J. Zinkle, C. Kinoshita, Defect production in ceramics, Journal of Nuclear Materials 251 (1997) 200-217. https://doi.org/10.1016/S0022-3115(97)00224-9

[13] W.J. Weber, Models and mechanisms of irradiation-induced amorphization in ceramics, Nuclear Instruments & Methods in Physics Research Section B 166-167 (2000) 98-106. https://doi.org/10.1016/S0168-583X(99)00643-6

[14] L.W. Hobbs, Chapter 17. Radiation effects in analysis of inorganic specimens by TEM in Introduction to Analytical Electron Microscopy, J.J. Hren, J.I. Goldstein, D.C. Joy eds, Plenum ed., Plenum, New-York, 1979. https://doi.org/10.1007/978-1-4757-5581-7_17

[15] M.J. Berger, J.S. Coursey, M.A. Zucker, J. Chang, Stopping-power and range tables for electrons, protons, and helium ions, NIST, Physical Measurement Laboratory IUCR Report 37 and 49 (1984). http://www.nist.gov/pml/data/star/

[16] P.D. Lesueur, Cascades de déplacement dans les solides polyatomiques, Philosophical Magazine A 44(4) (1981) 905-929. https://doi.org/10.1080/01418618108239557

[17] W.A. Dollase, Correction of intensities for preferred orientation in powder diffractometry: application of the March Model, Journal of Applied Crystallography 19(4) (1986) 267-272. https://doi.org/10.1107/S0021889886089458

[18] M. Toplak, G. Birarda, S. Read, C. Sandt, S.M. Rosendahl, L. Vaccari, J. Demsar, F. Borondics, Infrared Orange: connecting hyperspectral data with machine learning, Synchrotron Radiations News 30(4) (2017) 40-45. https://doi.org/10.1080/08940886.2017.1338424

[19] J. Demšar, T. Curk, A. Erjavec, T. Hočevar, M. Milutinovič, M. Možina, M. Polajnar, M. Toplak, A. Starič, M. Stajdohar, L. Umek, L. Zagar, J. Zbontar, M. Zitnik, B. Zupan, Orange: data mining toolbox in Python, Journal of Machine Learning Research 14(1) (2013) 2349-2353. https://dl.acm.org/doi/abs/10.5555/2567709.2567736

[20] C. Drouet, Apatite Formation: Why It May Not Work as Planned, and How to Conclusively Identify Apatite Compounds, BioMed Research International 2013 (2013) 1-12. https://doi.org/10.1155/2013/490946

[21] J.C. Elliott, Structure and chemistry of the apatites and other calcium phosphate phases, Elsevier, Amsterdam, Vol 18 1994.

[22] R.A. Young, W.E. Brown, Structures of biological minerals in: G.H. Nancollas (Ed.) Dahlem Konferenzen : Biological Mineralization and Demineralization. Life Science Research Report 23, Springer-Verlag Berlin Heidelberg New York, Berlin, 1982, pp. 101-141. https://doi.org/10.1007/978-3-642-68574-3

[23] P. Gras, C. Rey, O. Marsan, S. Sarda, C. Combes, Synthesis and characterisation of hydrated calcium pyrophosphate phases of biological interest, European Journal of Inorganic Chemistry 34 (2013) 5886-5895. https://doi.org/10.1002/ejic.201300955

[24] A.O. McIntosh, W.L. Jablonski, X-ray diffraction powder patterns of calcium phosphates, Analytical Chemistry 28(9) (1956) 1424-1427. https://doi.org/10.1021/ac60117a019

[25] R.L. Frost, S.J. Palmer, Thermal stability of the 'cave' mineral brushite $CaHPO_4 \cdot 2H_2O$ – Mechanism of formation and decomposition, Thermochimica Acta 521 (2011) 14-17. https://doi.org/10.1016/j.tca.2011.03.035

[26] F. Casciani, R.A. Condrate, The vibrational spectra of brushite, $CaHPO_4.\ 2H_2O$, Spectroscopy Letters 12(10) (1979) 699-713. https://doi.org/10.1080/00387017908069196

[27] I.A. Karampas, C.G. Kontoyannis, Characterization of calcium phosphates mixtures, Vibrational Spectroscopy 64 (2013) 126-133. https://doi.org/10.1016/j.vibspec.2012.11.003

[28] R.L. Frost, Y. Xi, R.E. Pogson, G.J. Millar, K. Tan, S.J. Palmer, Raman spectroscopy of synthetic $CaHPO_4.2H_2O$- and in comparison with the cave mineral brushite, Journal of Raman Spectroscopy 43(4) (2012) 571-576. https://doi.org/10.1002/jrs.3063

[29] G. Penel, N. Leroy, P. van Landuyt, B. Flautre, P. Hardouin, J. Lemaitre, G. Leroy, Raman microspectrometry studies of brushite cement: in vivo evolution in a Sheep model, Bone 25(2) (1999) 81S-84S. https://doi.org/10.1016/S8756-3282(99)00139-8

[30] J. Soulié, P. Gras, O. Marsan, D. Laurencin, C. Rey, C. Combes, Development of a new family of monolithic calcium (pyro)phosphate glasses by soft chemistry, Acta Biomaterialia 41 (2016) 320-327. https://doi.org/10.1016/j.actbio.2016.05.030

[31] B.C. Cornilsen, Solid state vibrational spectra of calcium pyrophosphate dihydrate, Journal of Molecular Structure 117(1-2) (1984) 1-9. https://doi.org/10.1016/0022-2860(84)87237-3

[32] J. Xu, I.S. Butler, D.F.R. Gilson, FT-Raman and high-pressure infrared spectroscopic studies of dicalcium phosphate dihydrate ($CaHPO_4 \cdot 2H_2O$) and anhydrous dicalcium phosphate ($CaHPO_4$), Spectrochimica Acta A 55(14) (1999) 2801-2809. https://doi.org/10.1016/S1386-1425(99)00090-6

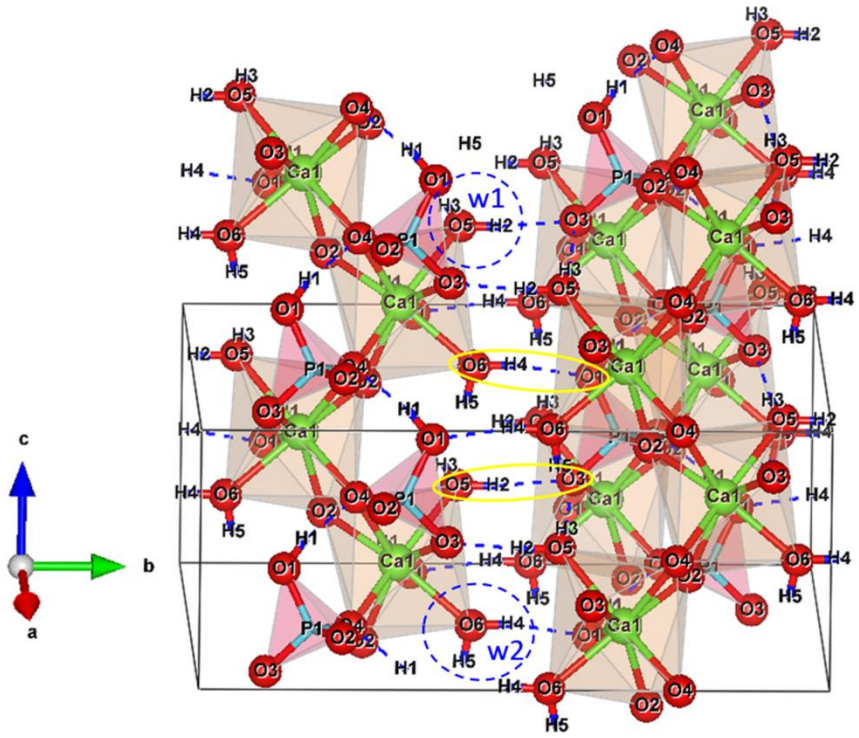

Fig. 1. *Crystal structure of brushite $CaHPO_4 \cdot 2H_2O$ viewed parallel to the (**b**,**c**) plane. The H atoms (dark blue) are numbered H1 to H5. The phosphate units are shown as solid light purple tetrahedra. The H1 inside the blue circle refers to the acidic proton (HPO_4) of the structure. The Ca atoms (shaded light green) are at the center of the CaO_8 polyhedra with the O atoms (red) numbered O1 to O6. The blue ellipses highlight two non-identical distorted water molecules, referred to as w1 and w2. The yellow ellipses indicate the hydrogen bonds that bind parallel layers.*

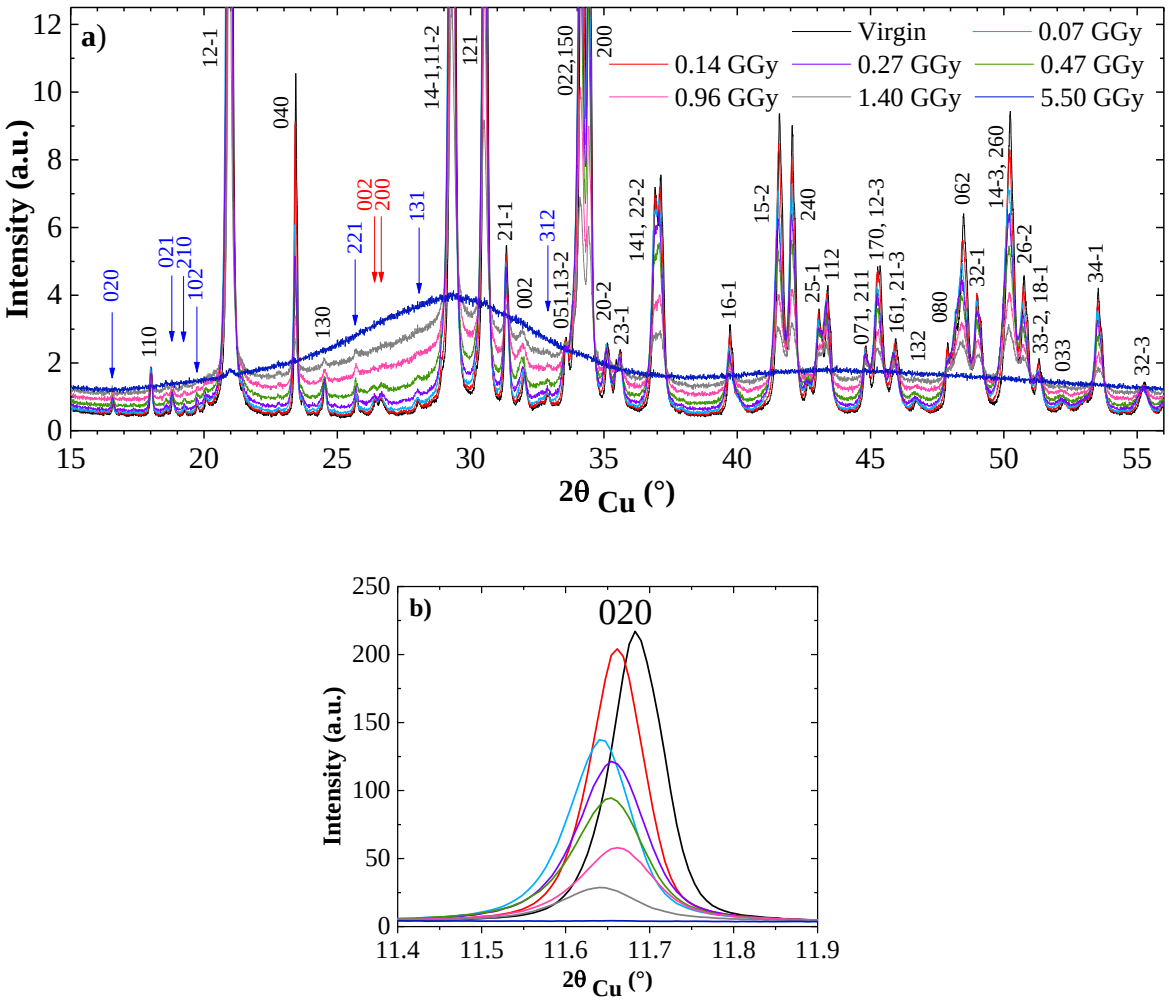

***Fig. 2**. Powder X-ray diffraction patterns of virgin and irradiated brushite, $CaHPO_4.2H_2O$, at different doses from 0.07 GGy to 5.5 GGy in two angular windows from $2\theta_{Cu}$ = 15 to 55° (a) and $2\theta_{Cu}$ = 11 to 12.5° (b). All hkl Bragg lines of the respective phases are indicated in black for brushite, in red for monetite and in blue for newberyte. Note the diffuse background scattering increasing with dose until the highest one (5.5 GGy).*

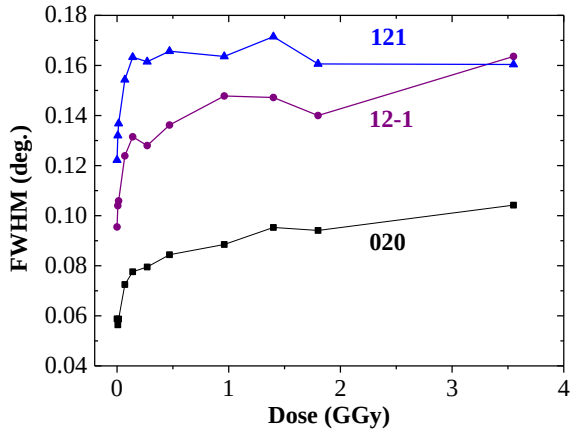

***Fig. 3**. Evolution of the peak broadening (FWHM) of three intense peaks of brushite (020, 12-1 and 121 Bragg lines) as a function of the radiation dose.*

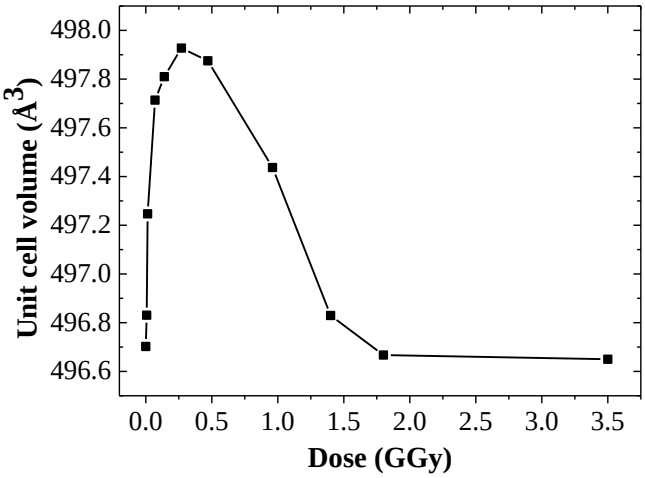

***Fig. 4**. Evolution of the unit cell volume of brushite as a function of the irradiation dose.*

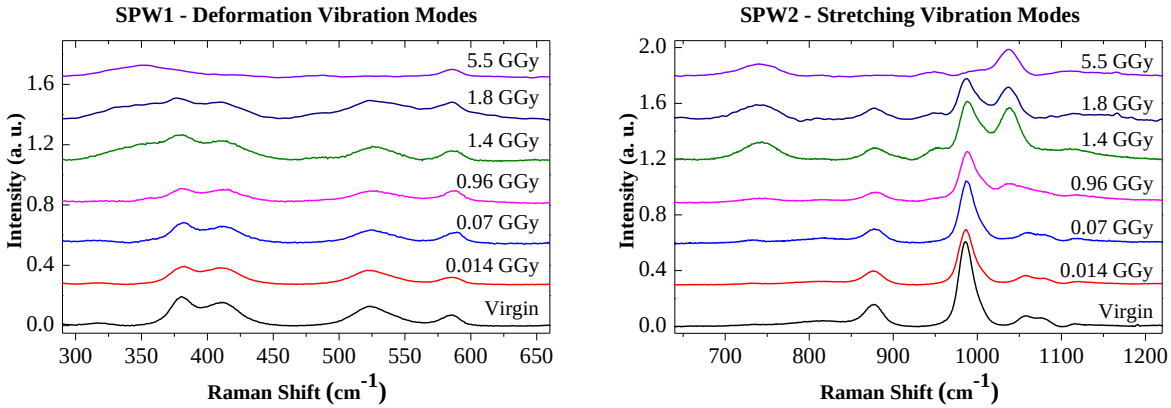

***Fig. 5**. Raman spectra of six samples irradiated at different doses and of virgin brushite. All spectra have been shifted with respect to each other to facilitate visualization. Spectral windows 1 and 2 correspond to left and right panels respectively.*

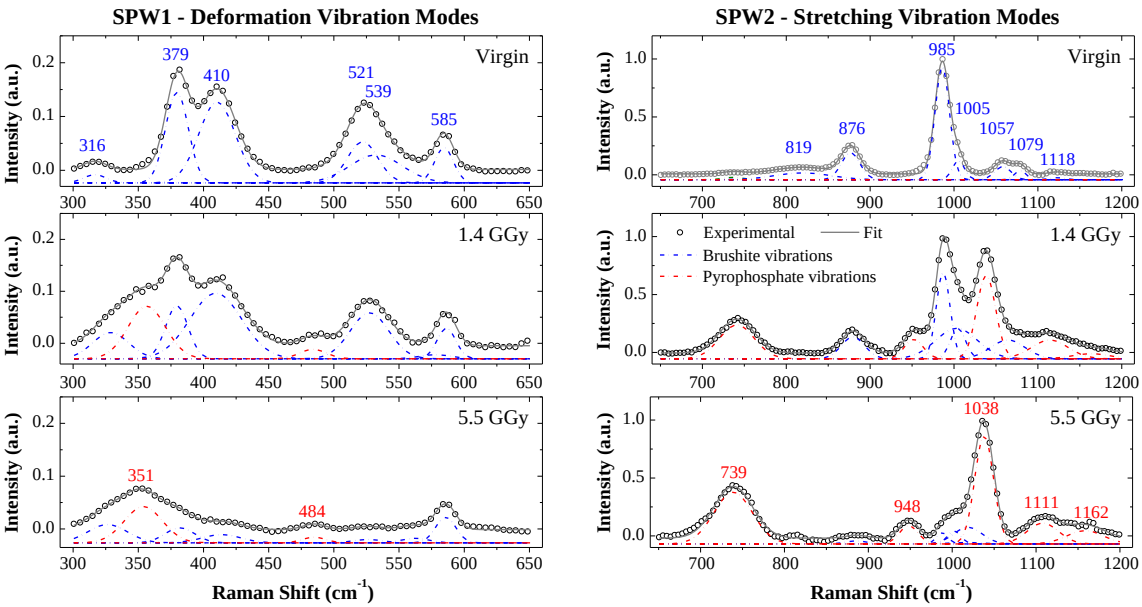

Fig. 6. *Experimental and fitted spectra corresponding to virgin and irradiated samples at 1.4 and 5.5 GGy in spectral window 1 (SPW1). The individual Gaussian peaks used to fit the experimental data are shown in either blue or red to identify them with brushite or pyrophosphate respectively. Idem for data in spectral window 2 (SPW2).*

Table 1. Density ρ, mean excitation energy *I*, total inelastic stopping power and CSDA range R estimated using ESTAR [15] for brushite and 2.5 MeV electrons.

Density ρ (g/cm^3)	*I* (eV)	$-\left[\frac{dE}{dx}\right]_{inel}$ (MeV/cm)	R (mm)
2.32	78.3	4.3	5.6

Table 2. Irradiation conditions using the SIRIUS platform for 2.5 MeV electrons. The electron doses are calculated without taking into account the contribution of backscattered electrons and the absorption effects along the trajectory. The absorbed doses are calculated using the inelastic stopping power values estimated using ESTAR [15]. The ion displacements damages, in dpa, are given assuming, for sake of simplicity, a value of displacement cross section (in barn), σ_d, equal to 20 b at 2.5 MeV for all three calcium, phosphorous and oxygen ions, which is the order of magnitude found using the SMOTT/POLY code proposed by D. Lesueur [16] for an hypothetical threshold displacement energy value, E_d of order 60 eV for all three ions.

Dose (C)	0.005	0.01	0.05	0.1	0.2	0.35	0.7	1	1.3	4
Fluence ($e^-.cm^{-2}$) x 10^{18}	0.0023	0.0047	0.2346	0.4693	0.9386	1.643	3.285	4.697	6.101	18.77
Dose (GGy)	0.007	0.014	0.07	0.14	0.27	0.47	0.96	1.40	1.78	5.50
Dose (dpa) x 10^{-5}	0.05	0.08	0.47	0.94	1.9	3.3	6.6	9.4	13	38